

*Radiative effect of two contrail cirrus outbreaks over Western Europe estimated using geostationary satellite observations and radiative transfer calculations*

Article

Published Version

Creative Commons: Attribution-Noncommercial-No Derivative Works 4.0

Open Access

Wang, X., Wolf, K., Boucher, O. and Bellouin, N. ORCID: <https://orcid.org/0000-0003-2109-9559> (2024) Radiative effect of two contrail cirrus outbreaks over Western Europe estimated using geostationary satellite observations and radiative transfer calculations. *Geophysical Research Letters*, 51 (7). e2024GL108452. ISSN 0094-8276 doi: <https://doi.org/10.1029/2024GL108452> Available at <https://centaur.reading.ac.uk/115856/>

It is advisable to refer to the publisher's version if you intend to cite from the work. See [Guidance on citing](#).

To link to this article DOI: <http://dx.doi.org/10.1029/2024GL108452>

Publisher: American Geophysical Union

All outputs in CentAUR are protected by Intellectual Property Rights law, including copyright law. Copyright and IPR is retained by the creators or other copyright holders. Terms and conditions for use of this material are defined in the [End User Agreement](#).

[www.reading.ac.uk/centaur](http://www.reading.ac.uk/centaur)

**CentAUR**

Central Archive at the University of Reading

Reading's research outputs online

# Geophysical Research Letters®



## RESEARCH LETTER

10.1029/2024GL108452

### Key Points:

- The cloud radiative effect (CRE) of two successive contrail-cirrus outbreaks is estimated from geostationary satellite measurements
- These two outbreaks have different CRE sign and magnitude, which can be explained by their different cloud properties and time evolutions
- The study suggests that automated quantification of contrail-cirrus CRE for monitoring or verification of contrail avoidance is feasible

### Supporting Information:

Supporting Information may be found in the online version of this article.

### Correspondence to:

X. Wang,  
xinyue.wang@ipsl.fr

### Citation:

Wang, X., Wolf, K., Boucher, O., & Bellouin, N. (2024). Radiative effect of two contrail cirrus outbreaks over Western Europe estimated using geostationary satellite observations and radiative transfer calculations. *Geophysical Research Letters*, 51, e2024GL108452. <https://doi.org/10.1029/2024GL108452>

Received 9 NOV 2023

Accepted 23 MAR 2024


### Author Contributions:

**Conceptualization:** Xinyue Wang, Olivier Boucher, Nicolas Bellouin  
**Data curation:** Xinyue Wang  
**Formal analysis:** Xinyue Wang  
**Funding acquisition:** Olivier Boucher, Nicolas Bellouin  
**Investigation:** Xinyue Wang, Nicolas Bellouin  
**Methodology:** Xinyue Wang, Kevin Wolf, Olivier Boucher, Nicolas Bellouin  
**Software:** Xinyue Wang, Kevin Wolf, Olivier Boucher  
**Supervision:** Olivier Boucher, Nicolas Bellouin

© 2024. The Authors.

This is an open access article under the terms of the [Creative Commons Attribution-NonCommercial-NoDerivs License](#), which permits use and distribution in any medium, provided the original work is properly cited, the use is non-commercial and no modifications or adaptations are made.

## Radiative Effect of Two Contrail Cirrus Outbreaks Over Western Europe Estimated Using Geostationary Satellite Observations and Radiative Transfer Calculations

Xinyue Wang<sup>1</sup> , Kevin Wolf<sup>1,2</sup>, Olivier Boucher<sup>1</sup> , and Nicolas Bellouin<sup>1,3</sup> 

<sup>1</sup>Institut Pierre–Simon Laplace, Sorbonne Université/CNRS, Paris, France, <sup>2</sup>Institute for Meteorology, Leipzig University, Leipzig, Germany, <sup>3</sup>Department of Meteorology, University of Reading, Reading, UK

**Abstract** Estimation of the perturbation to the Earth's energy budget by contrail outbreaks is required for estimating the climate impact of aviation and verifying the climate benefits of proposed contrail avoidance strategies such as aircraft rerouting. Here we identified two successive large-scale contrail outbreaks developing in clear-sky conditions in geostationary and polar-orbiting satellite infrared images of Western Europe lasting from 22–23 June 2020. Their hourly cloud radiative effect, obtained using geostationary satellite cloud retrievals and radiative transfer calculations, is negative or weakly positive during daytime and positive during nighttime. The cumulative energy forcing of the two outbreaks is 7 PJ and −8.5 PJ, with uncertainties of 3 PJ, stemming each from approximately 15–20 flights over periods of 19 and 7 hr, respectively. This study suggests that an automated quantification of contrail outbreak radiative effect is possible, at least for contrails forming in clear sky conditions.

**Plain Language Summary** Contrail cirrus is produced by aircraft and perturb the energy budget of the Earth. However, the actual size of the perturbation is uncertain. In this study, we calculate the energy budget perturbation of two successive contrail-cirrus outbreaks over Western Europe from 22–23 June 2020. An infrared image composite allows the identification and tracking of contrails with a 15 min frequency, which is verified by comparison to satellite images with better horizontal resolution from several polar-orbiting platforms. Cloud properties of the contrail-cirrus clusters, estimated from geostationary satellite data, are used in radiative transfer calculations. We find that one contrail cirrus outbreak adds an average power of 2 TW over 20 hr, while the other removes 3.3 TW over 8 hr. This cumulative energy depends on the lifespan and cloud properties of the outbreaks. This case study suggests that geostationary satellite observations allow the estimation of the energy perturbation of a contrail outbreak, with encouraging implications for contrail-cirrus monitoring and the verification of contrail avoidance strategies.

## 1. Introduction

Large uncertainties remain in the impact of cirrus clouds on the top of atmosphere (TOA) radiation budget, especially when perturbations caused by anthropogenic activities, such as contrail (condensation trail) cirrus, are considered (Kärcher, 2018; Lee et al., 2021). Cirrus is an ice cloud formed either homogeneously from supercooled liquid droplets or heterogeneously in ice supersaturated regions (ISSR) when ice-nucleating aerosols are present (Heymsfield et al., 2017; Kärcher et al., 2022). Contrails form differently: liquid droplets develop from cloud condensation nuclei behind aircraft engines when water vapor is supersaturated with respect to liquid water and then freeze into ice crystals. Contrails that form in ISSRs persist, spread, and may merge into contrail-cirrus (Burkhardt & Kärcher, 2011; Schumann et al., 2017), which increases the amount of cirrus. The cloud radiative effect (CRE) of contrail-cirrus greatly exceeds that of young and linear contrails (Voigt et al., 2011) and adds to the total warming effect caused by aviation (Lee et al., 2021), prompting calls for rerouting flights away from ISSRs to avoid persistent contrail formation (Immler et al., 2008; Irvine et al., 2012; Mannstein et al., 2005; Teoh et al., 2020). However, the current uncertainty in the contrail-cirrus radiative effect means that it would be difficult to quantify the climate benefit, if any, of such avoidance schemes.

Cirrus clouds reflect incident shortwave (SW) radiation back to space while they absorb and emit longwave (LW) radiation within the Earth's atmosphere, resulting in compensating SW and LW CREs and a positive net CRE on a global, annual average (Burkhardt et al., 2018; Chen et al., 2000; Gettelman et al., 2021; Lee et al., 2021; Rädcl & Shine, 2008). At smaller spatio-temporal scales, the radiative forcing due to contrail cirrus outbreaks, which is the

**Validation:** Xinyue Wang, Kevin Wolf, Olivier Boucher, Nicolas Bellouin  
**Visualization:** Xinyue Wang  
**Writing – original draft:** Xinyue Wang  
**Writing – review & editing:** Kevin Wolf, Olivier Boucher, Nicolas Bellouin

main contributor (Burkhardt & Kärcher, 2009) to contrail induced warming effects, exhibits large variations (in both sign and magnitude) due to variations in solar zenith angle, surface albedo, temperature of underlying surfaces, etc (Wolf et al., 2023), and therefore needs to be further explored (Bier et al., 2017; Schumann et al., 2012), ideally for different regions and seasons (Duda et al., 2001, 2004, 2019), to get a better understanding of their features, support contrail-cirrus cloud modeling, and determine the potential for quantifying and monitoring contrail outbreaks' CRE from observations.

Algorithms for tracking individual contrails and estimation of their radiative forcing have been proposed by Vazquez-Navarro et al. (2010, 2015). Haywood et al. (2009) investigated a persistent contrail with a distinct, spiral-shaped pattern that evolved into contrail cirrus near the United Kingdom in March 2009. The net radiative effect of the contrail cirrus was estimated to be  $30 \text{ W m}^{-2}$  during the nighttime hours between 11 and 20 UTC on the day of interest, while its daytime counterpart was  $10 \text{ W m}^{-2}$  on average. Although Haywood et al. (2009) brought strong evidence from spatial coherence and modeling that at least a fraction of their observed cirrus was of anthropogenic origin, that fraction could not be quantified. This is a common difficulty for satellite-based studies that cannot provide a counterfactual situation against which the observed scenes can be contrasted. Schumann and Graf (2013) suggested that aviation-induced cirrus could be distinguished from natural cirrus by linking the former to the diurnal cycle of air traffic. More recently, Wang et al. (2023) examined a contrail cirrus case which lasted around 8 hr over the North Atlantic on 26 March 2014, by using a combination of aircraft measurements of ice microphysics, lidar observations of cloud and aerosol backscatter profiles, and cirrus properties based on geostationary satellite observations.

In the present study, we identify and analyze a 2-day case composed of two contrail-cirrus outbreaks that persist over Western Europe for more than 24 hr from 22–23 June 2020. This occurred during a time of relatively low aircraft traffic due to the COVID-19 pandemic, yet the outbreak is substantial, and as such provides a good opportunity to assess quantitatively a complete diurnal variation of contrail-cirrus CRE at hourly resolution. In Section 2, we introduce the data and methods used for investigation; the results are interpreted in Section 3, and a conclusion with discussion follows in Section 4.

## 2. Data and Method

### 2.1. Data

#### 2.1.1. Data From Geostationary Scanning of SEVIRI/MSG

Contrail cirrus tracking is achieved using the so-called Dust RGB (Red, Green, Blue) composite based on infrared window channels (8.7, 10.8, and  $12.0 \mu\text{m}$ ) of the Spinning Enhanced Visible and InfraRed Imager (SEVIRI) onboard the Meteosat Second Generation (MSG) satellite (Schmetz et al., 2002). Dust RGB images, although designed to detect plumes of mineral dust, are also suitable for the identification of cold, thin clouds, like contrail cirrus, as they provide excellent brightness temperature contrast between high-level clouds and the surface, liquid clouds, or even mid-level thick ice clouds, making the movement of cirrus smoothly distinguishable and trackable. SEVIRI provides rapid scans every 15 min, both day and night, with 12 spectral bands and a 3 km spatial resolution at nadir point (corresponding to a  $\sim 4.5\text{--}5 \text{ km}$  resolution over Western Europe).

The Optimal Cloud Analysis (OCA; EUMETSAT, 2022) product is based on SEVIRI spectral measurements and determined using a radiative transfer model-based optimal estimation approach (Rodgers, 2000). OCA retrievals have the same spatial resolution as the original SEVIRI images and are operationally available at hourly frequency. OCA provides the cloud parameters needed for radiative transfer simulation, such as Cloud Optical Depth (COD, given at  $0.55 \mu\text{m}$ ), Cloud Top Pressure (CTP), and Cloud Effective Radius (CER) of both liquid droplets and ice crystals, as well as indicators of the cloud phase (liquid or ice).

#### 2.1.2. Polar Orbiting Satellite Observations

High resolution images of polar orbiting measurement are obtained from the Advanced Very High Resolution Radiometer (AVHRR; Kalluri et al., 2021) onboard the Meteorological Operational (MetOp) satellite program from the European Organisation for the Exploitation of Meteorological Satellites (EUMETSAT). AVHRR scans the whole Earth twice a day with 6 spectral bands having a 1.1 km spatial resolution. Here we use the brightness temperature difference (BTD) of thermal infrared bands 4 ( $10.30\text{--}11.30 \mu\text{m}$ ) and 5 ( $11.50\text{--}12.50 \mu\text{m}$ ) for contrail cirrus detection. AVHRR produces different types of imagery with spatial resolutions of 1.1 and 4 km. In this

study, the Full Resolution Area Coverage (FRAC; 1.1 km) data from MetOp-B and -C is selected. We supplement AVHRR images with observations from the Visible Infrared Imaging Radiometer Suite (VIIRS; Cao et al., 2013) onboard the Suomi National Polar-Orbiting Partnership (Suomi-NPP) platform. VIIRS has 22 bands with different spatial resolutions of 375 and 750 m, and wavelengths ranging from 412 nm to 12  $\mu\text{m}$ . The BTD between VIIRS's thermal infrared bands 15 (10.8  $\mu\text{m}$ ) and 16 (12.0  $\mu\text{m}$ ) closely matches that of AVHRR but with a higher spatial resolution of 750 m at nadir. The combination of the three satellites provides images at 10:09 and 12:11 UTC on 22 June, and 08:33 and 10:43 UTC on 23 June 2020.

## 2.2. Radiative Transfer Model

Radiative transfer simulations were performed with ecRad, which is the radiative transfer code used in the Integrated Forecasting System (IFS) of the European Center for Medium-Range Weather Forecasts (ECMWF; Hogan & Bozzo, 2018). We used the Tripleclouds solver (Shonk & Hogan, 2008) that allows calculation of vertical profiles of irradiances for all spectral bands. Detailed information of each LW and SW band can be found on Tables 2.3–4 of ECMWF (2023). For the parameterization of ice crystal optical properties, ecRad is configured to use the Fu-IFS scheme (Fu, 1996; Fu et al., 1998; Sun & Fu, 2001) which assumes a pristine hexagonal column habit for the ice crystals and has been operationally applied in the ECMWF IFS. Two other ice optics models (Baran et al., 2016; Yi et al., 2013) are available, but their impact on CRE is small since these bulk parameterizations consider a mixture of ice particle shapes, smoothing out the effects from specific ice shapes. Furthermore, Wolf et al. (2023) quantified the relative uncertainties from different input parameters and found the shape effect to be small when compared to other effects like effective radius and underlying surface albedo (their Figure 2).

The ecRad model requires the input data to be 3D and distributed over 137 pressure levels. The CRE was computed for each satellite pixel of the region of interest (8°W–4°E, 40°N–47.5°N) with an hourly timestep. For each column's calculation, we fed ecRad with the following data.

- Cloud properties were directly obtained from the OCA retrievals of COD, CER, and cloud fraction. The input cloud water mixing ratio ( $q$ , g/kg) was computed from COD, CER ( $\mu\text{m}$ ), and cloud layer depth in meter ( $\Delta Z$ ). To get  $\Delta Z$ , cloud layer pressure  $P_{cld}$  (hPa) is first obtained by approximating CTP to the nearest pressure level of ERA5, then we define the cloud layer pressure thickness ( $\Delta p$ ; hPa) as the difference between  $P_{cld}$  and the pressure of one layer above, then  $\Delta Z$  is derived from  $\Delta p$  from the hydrostatic law. By assuming that the cloud is homogeneous, the liquid water content (LWC,  $\text{g/m}^3$ ) is calculated by the equation below (Stephens, 1978)

$$\text{LWC} = \frac{2}{3} \frac{\text{COD} \times \text{CER}}{\Delta Z} \times 1000 \quad (1)$$

and the same equation is used for the computation of ice water content. Then,  $q$  is calculated with the equation below (MacVean and Mason (1990))

$$q = \frac{\text{LWC} \times R_{dry} \times T_{cld} \times (1 + 0.608 \times q_H)}{P_{cld}} \quad (2)$$

where  $R_{dry}$  denotes the ideal gas constant for dry air (287.1 J K<sup>-1</sup> kg<sup>-1</sup>),  $T_{cld}$  is the temperature (K) at  $P_{cld}$ , taken from the temperature profile described below, and  $q_H$  denotes the specific humidity (g/kg) from ERA5. Liquid and ice clouds are distinguished by two-dimensional pixel flags in OCA, so independent processing of their properties is possible when preparing the ecRad inputs. After horizontal separation, we assume the entire column has the same cloud phase. Ice CODs were increased from their original OCA values with a multiplicative factor of 1.3 to correct for a negative bias of 20%–30% reported in the OCA product documentation (EUMETSAT, 2022) after validation against the DARDAR product (raDAR-liDAR; Delanoë & Hogan, 2008, 2010) for the COD of ice clouds at high altitudes.

- Input atmospheric profiles of temperature and specific humidity are obtained from the ECMWF Reanalysis version 5 (ERA5; Hersbach et al., 2023) hourly distributions on pressure levels. These variables were vertically interpolated to the 137 vertical levels of ecRad. The input surface albedo for the 6 shortwave bands

is also from ERA5 with the UV visible albedo filling the first three ecRad wavebands with wavelengths ranging from 0.25 to 0.69  $\mu\text{m}$  and near IR albedo filling the next 3 wavebands for wavelengths 0.69–2.38  $\mu\text{m}$ .

The above procedures are repeated when calculating the energy forcing with uncertainties propagated from each input cloud property. Ice-COD uncertainties are capped at 0.6 and Ice-CTP uncertainties are capped at 140 hPa, following Section 3.7 of EUMETSAT (2022). Detailed interpretation of the energy forcing is presented in Section 3.2.

### 3. Results

#### 3.1. Visualization of the 22–23 June 2020 Outbreaks

Figure 1 shows the BTD from several polar orbiting platforms for four different times on 22–23 June over the region of interest. Contrails first become visible as linear shapes around 10 UTC on 22 June over northern Spain and the Bay of Biscay (Figure 1a), then grow, spread, and merge into contrail cirrus, which are then advected northeastward over France. Following that first outbreak, another outbreak appears around 0830 UTC on 23 June over the Bay of Biscay and northwestern France, around Brittany, as shown in Figures 1e and 1g. Figure S1 in Supporting Information S1 shows MODIS true color images of the two outbreaks, which qualitatively suggests that contrail cirrus in the second outbreak is optically thicker than in the first.

Despite the coarser spatial resolution of SEVIRI, its Dust RGB can observe the contrail cirrus and even thinner line-shaped contrails that are visible in the higher resolved data from the polar-orbiting instruments, as shown on the right column of Figure 1. The high consistency of contrail patterns at different moments between the SEVIRI Dust RGB images and polar-orbiting satellite observations confirms the reliability of the spatial resolution of the SEVIRI Dust RGB for contrail cirrus detection and tracking. It is very likely that both SEVIRI and the polar-orbiting imagers miss the younger stages of contrail formation (Vázquez-Navarro et al., 2015), when contrails are only tens of meters wide, but those stages have a negligible climate impact (Kärcher, 2018).

#### 3.2. Diurnal Variation of the Ice CRE

Figure 2 shows the ecRad-simulated, top-of-atmosphere, net (SW + LW) ice CRE patterns of the first contrail-cirrus cluster from 09 to 22 UTC on 22 June 2020. The corresponding video is shown at hourly intervals on the third panel of Video S1. This contrail outbreak lasted for  $\sim 18$  hr. During daylight hours from 06 to 18 UTC, the cooling effect in the solar spectrum generally dominates and the net ice CRE is negative. Then its sign switches abruptly around 19 UTC, when the solar zenith angle approaches  $90^\circ$ , indicating sunset. The net CRE is a balance between a negative CRE in the shortwave spectrum and a positive CRE in the LW spectrum. To better understand the variations of the sign of the net CRE, SW and LW CRE distributions are shown in Figures S4 and S5 in Supporting Information S1, respectively.

Daytime net CRE is dominated by SW cooling. However, there are also locations where the LW warming effect dominates, especially over land surfaces, as shown in Figures 2b and 2d. For a given COD, the SW CRE depends on the contrast between contrail albedo and surface albedo. LW CRE depends on the contrast between brightness temperature of clouds and that of the underlying surface. In Figure S4d in Supporting Information S1, a smaller contrast in albedo over land, where surface albedo is larger than ocean albedo, leads to a weaker cooling effect than for ocean-based contrails, resulting in a net warming over land. Focusing on ocean-based contrails only, where surface albedo is lower, Figure S4 in Supporting Information S1 shows a time dependence in SW CRE. This is because the reflection of sunlight by ice crystals depends on SZA and is maximum for SZA around  $70^\circ$ – $80^\circ$  (see Figure 8 of Schumann et al., 2012), so the SW cooling effect is stronger at 15 and 18 UTC than 12 UTC as shown in Figures S4c and S4d in Supporting Information S1. From late afternoon at  $\sim 18$  UTC, along with the reduction of solar radiation, the cooling effect - especially that over land surfaces - decreases. After 19 UTC and throughout the night, there is only LW warming effect until SW cooling appears again on the next morning at  $\sim 06$  UTC.

Figure 2 also shows that nighttime longwave warming is much larger than daytime net cooling. To get a quantitative estimate of the diurnal ice CRE, Figure 3b presents the hourly net total (i.e., spatially integrated) power of the ice CRE, in terawatts (TW) calculated as the sum over the pixels of the CRE in  $\text{W}/\text{m}^2$  multiplied by their surface areas. The integral is done over all ice cloud pixels in the region of interest. On the night of 22 June, the total ice CRE power reaches  $\sim 0.6$  TW, while during daylight hours, it peaks at  $\sim -0.4$  TW. This daytime

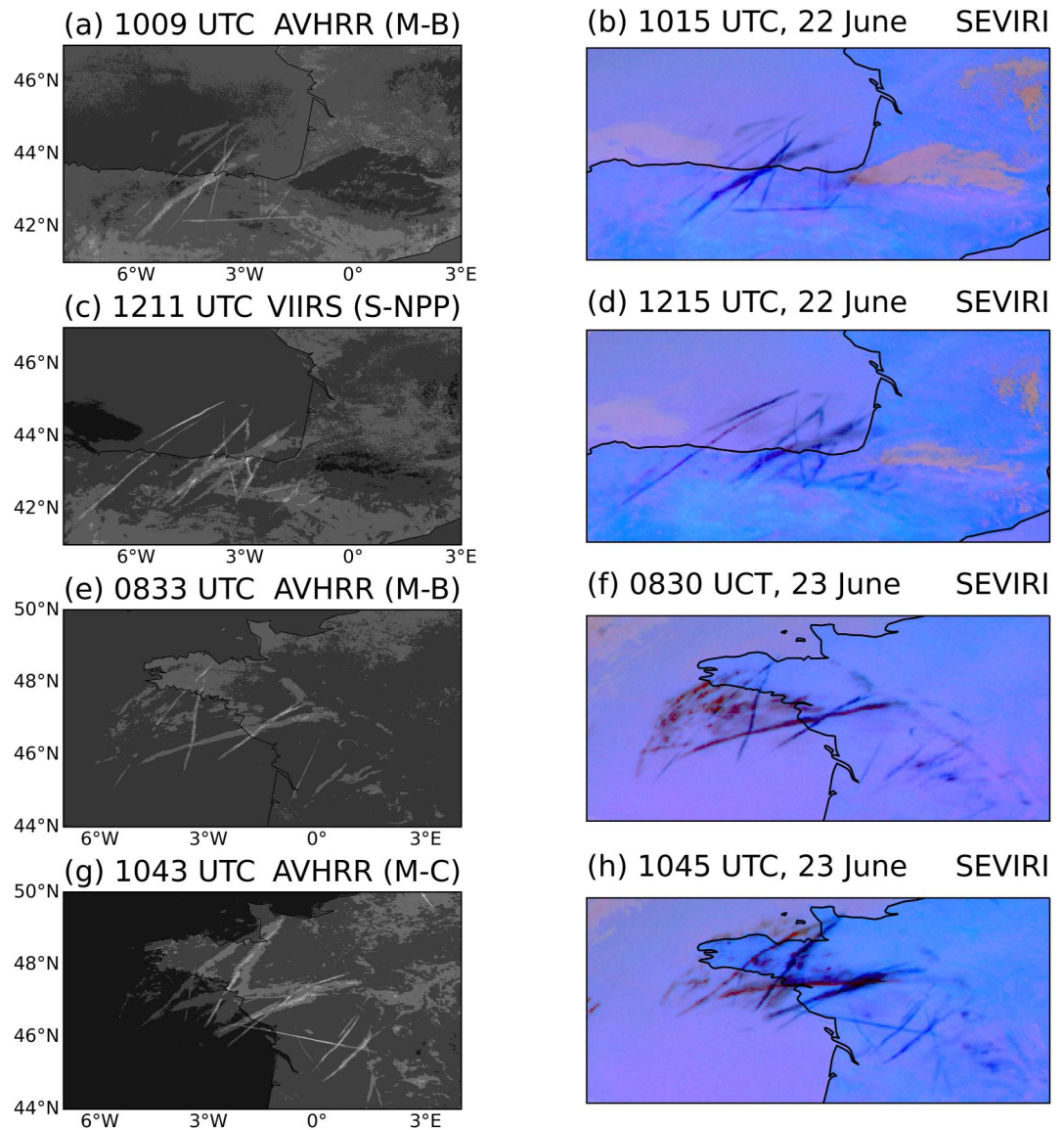


**Figure 1.** Brightness temperature difference images (left column) showing linear contrails and contrail-cirrus observed by polar orbiting satellite imagers AVHRR and VIIRS, onboard MetOp-B (M-B), MetOp-C (M-C), and Suomi-NPP (S-NPP) compared to those observed by the SEVIRI Dust RGB infrared composite (right column) at the closest observing time. The first two rows show images on 22 June, while the next two rows are for 23 June 2020. Grayscale images on the left column are brightness temperature differences between  $\sim 11$  and  $\sim 12$   $\mu\text{m}$  depending on the band wavelengths of the different imagers. Dark blue colors in the SEVIRI Dust RGB indicate high and thin cirrus with no clouds below, while dark brown illustrates high thick ice clouds. There is a  $\sim 10$  min difference between the nominal time of SEVIRI and the time of observation over Europe, but that difference does not affect the identification of contrail cirrus patterns.

magnitude is similar for the second contrail outbreak, which appears from 06 UTC to 13 UTC on 23 June, after which it overlaps with convective clouds and can no longer be tracked.

To go beyond ice CRE and estimate contrail radiative forcing, one must distinguish between contrail cirrus and natural cirrus. Long-range aircraft normally fly around  $\sim 250$  hPa, corresponding to  $\sim 10$  km in altitude (Teoh et al., 2024). Contrail cirrus persist within ISSRs, which in ERA5 are mainly distributed above 300 hPa in this case. Based on these considerations, we tried to separate contrail cirrus from lower-level ice clouds, which are more likely to be of natural origin, by using 300 hPa as a threshold. Considering that (a) the coastal areas near or continental areas over France and Spain could have more air traffic at lower levels than over the mid North Atlantic and (b) there is often/a height difference between the flight altitude and the altitude where contrail cirrus

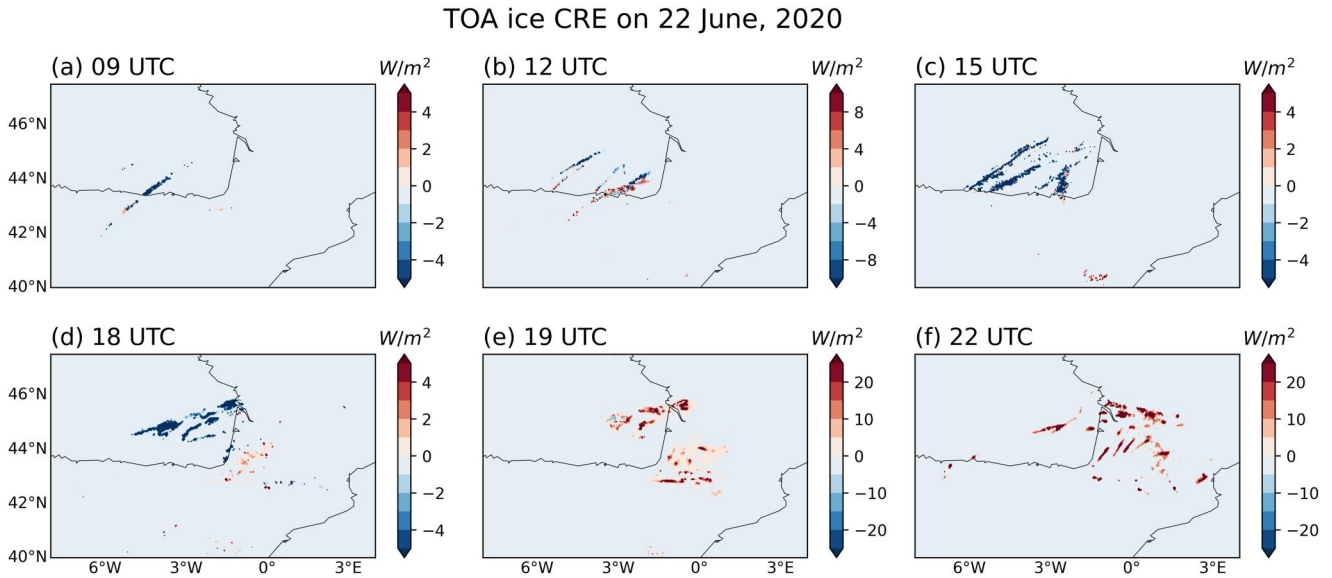


**Figure 2.** Distribution of ecRad-simulated, top-of-atmosphere, net (shortwave plus longwave) ice Cloud Radiative Effect (CRE), in  $W m^{-2}$ , over the focus region of this study, at different hours UTC from morning to night of 22 June 2020.

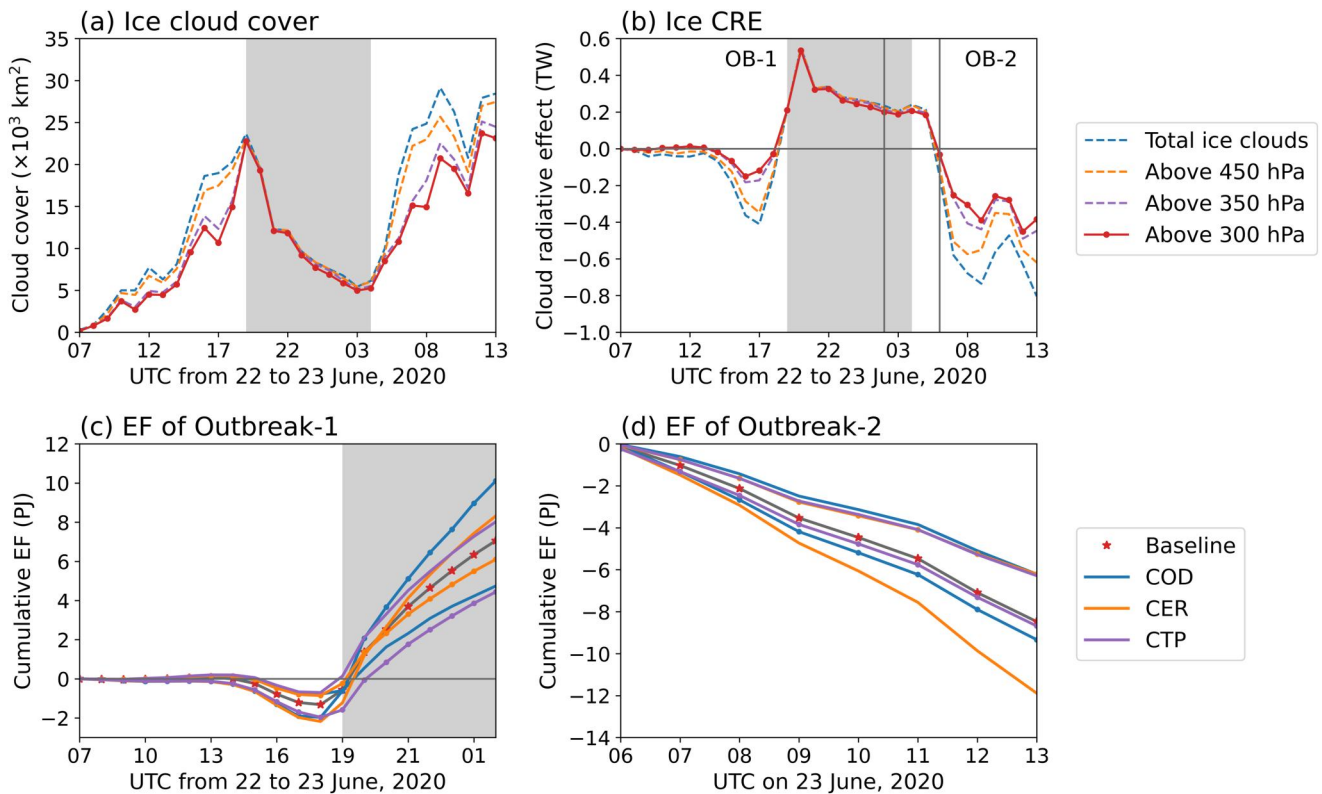


**Figure 3.** Time series of (a) ice cloud coverage, in  $10^3 km^2$ ; (b) net total power of the ice CRE, in terawatt (TW), over the region of interest, from 07 UTC on 22 June to 13 UTC on 23 June 2020, when persistent contrail cirrus is robustly observable from the SEVIRI Dust RGB imagery. Ice CRE in (b) are further converted to cumulative net energy forcing (EF) in petajoule (PJ), for two consecutive outbreaks: (c) Outbreak-1 from 07 UTC of 22 June to 02 UTC of 23 June, and (d) Outbreak-2 during daylight hours of 23 June 2020. The baseline EF is plotted with red stars in (c) and (d), while the EFs that account for uncertainties from input COD, CER, and CTP are shown in different colors. More specifically, colored lines with markers in (c) and (d) show calculations where cloud properties have been increased by the uncertainties, while lines without markers show results for cloud properties that have been decreased by the uncertainties. The gray background indicates nighttime.



eventually form because of the sinking of aircraft engine vortices and contrail sedimentation (Lewellen, 2014; Schumann et al., 2015), larger thresholds (lower altitudes) of 350 and 450 hPa are also applied to quantify the sensitivity of the net ice CRE and total power to the choice of altitude threshold. Furthermore climate models have suggested that contrail cirrus formation may affect natural cirrus (Bickel et al., 2020); but this cannot be diagnosed from observations alone. Therefore, discriminating contrail cirrus from natural cirrus remains imperfect.

Diurnal ice cloud cover evolution is shown in Figure 3a, the cloud cover increases from early morning to late afternoon, corresponding to simultaneously increased SW cooling (Figure S6a in Supporting Information S1) and LW warming (Figure S6b in Supporting Information S1), resulting in a relatively small net CRE from 07 UTC to ~14 UTC which increases to  $\sim -0.2$  TW at 16 UTC on 22 June, when SW cooling is stronger. COD shows a less pronounced variation (Figure S8 in Supporting Information S1), suggesting that the increase in cloud cover is not only due to an increase in available humidity but to the horizontal spreading of existing ice crystals. On the next morning, the ice cloud cover and the SW cooling increase again. Correspondingly, the net CRE starts to decrease at 04 UTC and changes sign to a net cooling at 06 UTC on 23 June.

The two consecutive outbreaks in this study have different life spans covering different periods of the day. To better quantify their climate impacts, we convert the ice-CRE in Figure 3b to an energy forcing (EF) with unit of petajoule (PJ,  $\times 10^{15}$  J), and plot the cumulative EF for these two outbreaks in Figures 3c and 3d, respectively. The first outbreak lasts from early morning to 02 UTC, its cumulative energy growing more negative during daytime, then switches to positive values at dusk, its cumulative energy over its lifetime ending positive at  $\sim 7$  PJ (Figure 3c). In contrast, the second outbreak appears during daytime and can be tracked for 7 hr. It has a cooling effect and its final cumulative EF is  $\sim -8.5$  PJ (Figure 3d), more than counteracting the perturbation of the first outbreak. Looking at the split in SW and LW contributions in Figure S7 in Supporting Information S1, the cumulative EF in the SW of Outbreak-2 is much larger than that of Outbreak-1, explaining the difference in the magnitude of their daytime net EF. This larger SW EF originates from optically thicker clouds in Outbreak-2, as already noted qualitatively from Figure S1 in Supporting Information S1 and shown quantitatively by the time series of mean-COD in Figure S8 in Supporting Information S1. Mean COD for Outbreak-1 is 0.3 and 0.6 for Outbreak-2. Furthermore, LW CRE saturates quicker than SW CRE with increasing COD, so the net (LW + SW) EF of Outbreak-2 during daytime is more negative than Outbreak-1.

Input cloud properties are uncertain, and their uncertainties are propagated to CRE calculations by increasing then decreasing COD, CER, and CTP in turn by their 1-sigma uncertainties estimated in the OCA product. Results for EF are shown in Figures 3c and 3d. For Outbreak-1, whose COD is smaller in general and therefore more uncertain, COD and CTP uncertainties propagate strongly to EF. The SW EF gets more negative when COD is increased (Figure S7a in Supporting Information S1). When CTP is increased, contrail cirrus moves lower down to warmer layers and their LW EF decreases because the temperature contrast with the surface decreases. For the second outbreak, which has larger ice COD, uncertainties are smaller and do not significantly change the resulting EF. CER uncertainties are relatively more important, especially when decreasing CER, because decreasing CER at constant COD implies more ice crystals, which have a stronger SW radiative effect. Taken independently, most of the uncertainties are within the range of  $[-3, 3]$  PJ for the two outbreaks. It is not possible to calculate a total uncertainty from individual uncertainties on COD, CER, and CTP, since the error covariances are unknown.

#### 4. Conclusion and Discussion

In this study, we focus on two contrail-cirrus outbreaks over western Europe, mainly Spain and France, that occurred on 22–23 June 2020 by using geostationary satellite observations and radiative transfer calculations. The two outbreaks appeared successively and persisted over 30 hr overall, providing us with an opportunity to monitor a complete diurnal variation of contrail outbreaks in terms of coverage and radiative forcing. The total power of the ice CRE of contrail cirrus above 300 hPa is 2.3 TW over 24 hr from 07 UTC of 22 June to the same time of the next day. When only looking at its night-time component, from 20 UTC of 22 June to 04 UTC of 23 June, the LW warming power is 2.5 TW.

The method used for quantification of the hourly radiative forcing of contrail outbreaks could be operationally applied for verifying the climate benefits of proposed strategies on contrail avoidance by aircraft rerouting (e.g., Grewe et al., 2017; Rosenow et al., 2018). A previous study (Teoh et al., 2020) reported an average contrail-cirrus power of 0.2 PJ per flight based on calculations with the Contrail Cirrus Prediction model (CoCiP) for six weeks

that included 26,534 flights forming contrails in Japanese airspace (see their Table 1). It is difficult to determine exactly the number of flights involved in the formation of the contrail outbreaks studied here. Counting the linear contrails that appear on Video S1 suggests there are ~15–20 flights involved in each outbreak. As a result, the absolute radiative power would be in the range of 0.4–0.6 PJ per flight but it is possible that some additional flights contribute to the outbreaks without leaving a clear signature. It is however important to remember that outbreaks are the product of several flights, which would need to be rerouted together if their radiative impact is to be avoided. That places limitations to the concept of individual flight rerouting.

The logical next step is therefore to automate the procedures we have used in this study, in the way illustrated by Figure S9 in Supporting Information S1, and scale up the monitoring to larger scales. Automation challenges could come from the automatic detection of linear contrails and identification of a contrail outbreak, but machine learning based systems are being developed (Hoffman et al., 2023; Ng et al., 2023). The current algorithm is suitable for contrail outbreaks that form in clear sky, in the absence of liquid clouds below. Cloudy-sky cases would need to be properly identified as two-layer systems in OCA. This will be investigated in a follow-up study. The radiative transfer calculation of ice CRE using ecRad takes about ~13 min on a 2.8 ~ GHz AMD EPYC 7402P CPU for one timeframe over the region of interest, which means a near-real time estimation of the CRE of local outbreaks could be made when cloud properties become available. The OCA product is already produced in near-real-time for MSG/SEVIRI and will become an operational product of the higher resolution MTG/FCI instrument (Spezzi et al., 2023). Finally, OCA can also be used with Himawari data, which increases the potential of our method to be generalized (Otsuka et al., 2021).

### Data Availability Statement

The dust RGB were composited with infrared measurements from the High Rate SEVIRI Level 1.5 Image Data, which is accessible from the EUMETSAT. The Polar-orbiting satellite observations used in Figure 1 are sourced from the archive of NOAA Comprehensive Large Array-data Stewardship System. Cloud properties were downloaded from the Optimal Cloud Analysis product of EUMETSAT (2022). The atmospheric information that used as input for radiative transfer simulations was taken from ERA5 (Hersbach et al., 2023). The images in Figure S1 in Supporting Information S1 were obtained using the EOSDIS worldview tool.

The study was performed using the following python modules: Numpy, Pytroll/Satpy, and h5py (analysis) and Matplotlib, Cartopy, and Basemap (visualization).

### Acknowledgments

We thank Steven Dewitte and Pierre de Buyl of Royal Meteorological Institute of Belgium for providing the GERB data. We appreciate the helpful discussion with Marie Doutriaux-Boucher and Alessio Bozzo at EUMETSAT on the use of OCA product. We acknowledge the Pytroll/Satpy team for their help on visualizing the polar-orbiting satellite images. This research has been supported by the French Ministère de la Transition Ecologique et Solidaire (Grant DGAC 382 N2021-39), with support from France's Plan National de Relance et de Resilience (PNRR) and the European Union's NextGenerationEU.

### References

- Baran, A. J., Hill, P., Walters, D., Hardiman, S. C., Furtado, K., Field, P. R., & Manners, J. (2016). The impact of two coupled cirrus microphysics–radiation parameterizations on the temperature and specific humidity biases in the tropical tropopause layer in a climate model. *Journal of Climate*, 29(14), 5299–5316. <https://doi.org/10.1175/jcli-d-15-0821.1>
- Bickel, M., Ponater, M., Bock, L., Burkhardt, U., & Reineke, S. (2020). Estimating the effective radiative forcing of contrail cirrus. *Journal of Climate*, 33(5), 1991–2005. <https://doi.org/10.1175/JCLI-D-19-0467.1>
- Bier, A., Burkhardt, U., & Bock, L. (2017). Synoptic control of contrail cirrus life cycles and their modification due to reduced soot number emissions. *Journal of Geophysical Research*, 122(21), 11584–11603. <https://doi.org/10.1002/2017jd027011>
- Burkhardt, U., Bock, L., & Bier, A. (2018). Mitigating the contrail cirrus climate impact by reducing aircraft soot number emissions. *npj Clim. Atmos. Sci.*, 1(1), 37. <https://doi.org/10.1038/s41612-018-0046-4>
- Burkhardt, U., & Kärcher, B. (2009). Process-based simulation of contrail cirrus in a global climate model. *Journal of Geophysical Research*, 114(D16), D16201. <https://doi.org/10.1029/2008JD011491>
- Burkhardt, U., & Kärcher, B. (2011). Global radiative forcing from contrail cirrus. *Nature Climate Change*, 1(1), 54–58. <https://doi.org/10.1038/nclimate1068>
- Cao, C., Luccia, F., Xiong, X., Wolfe, R., & Weng, F. (2013). Early on-orbit performance of the visible infrared imaging radiometer suite onboard the Suomi National Polar-Orbiting Partnership (S-NPP) satellite. *IEEE Transactions on Geoscience and Remote Sensing*, 52(2), 1142–1156. <https://doi.org/10.1109/tgrs.2013.2247768>
- Chen, T., Rossow, W. B., & Zhang, Y. (2000). Radiative effects of cloud-type variations. *Journal of Climate*, 13(1), 264–286. [https://doi.org/10.1175/1520-0442\(2000\)013<0264:reoctv>2.0.co;2](https://doi.org/10.1175/1520-0442(2000)013<0264:reoctv>2.0.co;2)
- Delanoë, J., & Hogan, R. J. (2008). A variational scheme for retrieving ice cloud properties from combined radar, lidar, and infrared radiometer. *Journal of Geophysical Research*, 113(D7), D07204. <https://doi.org/10.1029/2007JD009000>
- Delanoë, J., & Hogan, R. J. (2010). Combined CloudSat-CALIPSO-MODIS retrievals of the properties of ice clouds. *Journal of Geophysical Research*, 115(D4), D00H29. <https://doi.org/10.1029/2009JD012346>
- Duda, D., Minnis, P., & Nguyen, L. (2001). Estimates of cloud radiative forcing in contrail clusters using GOES imagery. *Journal of Geophysical Research*, 106(D5), 4927–4937. <https://doi.org/10.1029/2000jd900393>
- Duda, D., Minnis, P., Nguyen, L., & Palikonda, R. (2004). A case study of the development of contrail clusters over the Great Lakes. *Journal of the Atmospheric Sciences*, 61(10), 1132–1146. [https://doi.org/10.1175/1520-0469\(2004\)061<1132:acsotd>2.0.co;2](https://doi.org/10.1175/1520-0469(2004)061<1132:acsotd>2.0.co;2)

- Duda, D. P., Bedka, S. T., Minnis, P., Spangenberg, D. A., Khlopenkov, K., Chee, T., & Smith, W. L. (2019). Northern Hemisphere contrail properties derived from Terra and Aqua MODIS data for 2006 and 2012. *Atmospheric Chemistry and Physics*, 19(8), 5313–5330. <https://doi.org/10.5194/acp-19-5313-2019>
- ECMWF. (2023). IFS documentation CY48R1 - Part IV: Physical processes. *IFS Documentation CY48R1*, 4. <https://doi.org/10.21957/02054f0fbf>
- EUMETSAT. (2022). Optimal cloud analysis climate data record release 1 - MSG - 0 degree [Dataset]. *European Organisation for the Exploitation of Meteorological Satellites*. [https://doi.org/10.15770/EUM\\_SEC\\_CLM\\_0049](https://doi.org/10.15770/EUM_SEC_CLM_0049)
- Fu, Q. (1996). An accurate parameterization of the solar radiative properties of cirrus clouds in climate models. *Journal of Climate*, 9, 2058–2082. [https://doi.org/10.1175/1520-0442\(1996\)009<2058:aapots>2.0.co;2](https://doi.org/10.1175/1520-0442(1996)009<2058:aapots>2.0.co;2)
- Fu, Q., Yang, P., & Sun, W. (1998). An accurate parameterization of the infrared radiative properties of cirrus clouds in climate models. *Journal of Climate*, 11(9), 2223–2237. [https://doi.org/10.1175/1520-0442\(1998\)011<2223:aapoti>2.0.co;2](https://doi.org/10.1175/1520-0442(1998)011<2223:aapoti>2.0.co;2)
- Gottelman, A., Chen, C. C., & Bardeen, C. G. (2021). The climate impact of COVID-19-induced contrail changes. *Atmospheric Chemistry and Physics*, 21(12), 9405–9416. <https://doi.org/10.5194/acp-21-9405-2021>
- Grewe, V., Matthes, S., Frömming, C., Brinkop, S., Jöckel, P., Gierens, K., et al. (2017). Feasibility of climate-optimized air traffic routing for trans-Atlantic flights. *Environmental Research Letters*, 12(3), 034003. <https://doi.org/10.1088/1748-9326/aa5ba0>
- Haywood, J. M., Allan, R. P., Bornemann, J., Forster, P. M., Francis, P. N., Milton, S., et al. (2009). A case study of the radiative forcing of persistent contrails evolving into contrail-induced cirrus. *Journal of Geophysical Research*, 114(D24), D24201. <https://doi.org/10.1029/2009JD012650>
- Hersbach, H., Bell, B., Berrisford, P., Biavati, G., Horányi, A., Muñoz Sabater, J., et al. (2023). ERA5 hourly data on single levels from 1940 to present [Dataset]. *Copernicus Climate Change Service (C3S) Climate Data Store (CDS)*. <https://doi.org/10.24381/cds.adbb2d47>
- Heymsfield, A. J., Krämer, M., Luebke, A., Brown, P., Cziczo, D. J., Franklin, C., et al. (2017). Cirrus clouds. *Meteorological Monographs*, 58, 1–2. <https://doi.org/10.1175/amsmonographs-d-16-0010.1>
- Hoffman, J. P., Rahmes, T. F., Wimmers, A. J., & Feltz, W. F. (2023). The application of a convolutional neural network for the detection of contrails in satellite imagery. *Remote Sensing*, 15(11), 2854. <https://doi.org/10.3390/rs15112854>
- Hogan, R. J., & Bozzo, A. (2018). A flexible and efficient radiation scheme for the ECMWF model. *Journal of Advances in Modeling Earth Systems*, 10(8), 1990–2008. <https://doi.org/10.1029/2018ms001364>
- Immler, F., Treffeisen, R., Engelbart, D., Krüger, K., & Schrems, O. (2008). Cirrus, contrails, and ice supersaturated regions in high pressure systems at northern mid latitudes. *Atmospheric Chemistry and Physics*, 8(6), 1689–1699. <https://doi.org/10.5194/acp-8-1689-2008>
- Irvine, E. A., Hoskins, B. J., & Shine, K. P. (2012). The dependence of contrail formation on the weather pattern and altitude in the North Atlantic. *Geophysical Research Letters*, 39(12), L12802. <https://doi.org/10.1029/2012GL051909>
- Kalluri, S., Cao, C., Heidinger, A., Ignatov, A., Key, J., & Smith, T. (2021). The advanced very high resolution radiometer: Contributing to earth observations for over 40 years. *Bulletin American Meteorology Social*, 102(2), E351–E366. <https://doi.org/10.1175/bams-d-20-0088.1>
- Kärcher, B. (2018). Formation and radiative forcing of contrail cirrus. *Nature Communications*, 9(1), 1824. <https://doi.org/10.1038/s41467-018-04068-0>
- Kärcher, B., DeMott, P. J., Jensen, E. J., & Harrington, J. Y. (2022). Studies on the competition between homogeneous and heterogeneous ice nucleation in cirrus formation. *Journal of Geophysical Research*, 127(3), e2021JD035805. <https://doi.org/10.1029/2021jd035805>
- Lee, D. S., Fahey, D. W., Skowron, A., Allen, M. R., Burkhardt, U., Chen, Q., et al. (2021). The contribution of global aviation to anthropogenic climate forcing for 2000 to 2018. *Atmospheric Environment*, 244, 117834. <https://doi.org/10.1016/j.atmosenv.2020.117834>
- Lewellen, D. C. (2014). Persistent contrails and contrail cirrus. Part II: Full lifetime behavior. *Journal of the Atmospheric Sciences*, 71(12), 4420–4438. <https://doi.org/10.1175/JAS-D-13-0317.1>
- MacVean, M. K., & Mason, P. J. (1990). Cloud-top entrainment instability through small-scale mixing and its parameterization in numerical models. *Journal of the Atmospheric Sciences*, 47(8), 1012–1030. [https://doi.org/10.1175/1520-0469\(1990\)047<1012:cteits>2.0.co;2](https://doi.org/10.1175/1520-0469(1990)047<1012:cteits>2.0.co;2)
- Mannstein, H., Spichtinger, P., & Gierens, K. (2005). A note on how to avoid contrail cirrus. *Transportation Research Part D: Transport and Environment*, 10(5), 421–426. <https://doi.org/10.1016/j.trd.2005.04.012>
- Ng, J. Y. H., McCloskey, K., Cui, J., Brand, E., Sarna, A., Goyal, N., et al. (2023). OpenContrails: Benchmarking contrail detection on GOES-16 ABI. *arXiv preprint arXiv:2304.02122*.
- Otsuka, M., Seko, H., Hayashi, M., & Koizumi, K. (2021). Data validation and mesoscale assimilation of Himawari-8 optimal cloud analysis products. *Journal of Atmospheric and Oceanic Technology*, 38(2), 223–242. <https://doi.org/10.1175/jtech-d-20-0015.1>
- Rädel, G., & Shine, K. P. (2008). Radiative forcing by persistent contrails and its dependence on cruise altitudes. *Journal of Geophysical Research*, 113(D7), D07105. <https://doi.org/10.1029/2007JD009117>
- Rodgers, C. (2000). Inverse methods for atmospheric sounding. Theory and practice. *Series on atmospheric, oceanic and planetary physics*, 2. New Jersey: World Scientific. <https://doi.org/10.1142/3171>
- Rosenow, J., Fricke, H., Luchkova, T., & Schultz, M. (2018). Minimizing contrail formation by rerouting around dynamic ice-supersaturated regions. *Aeron Aero Open Access J*, 2(3), 105–111. <https://doi.org/10.15406/aaobj.2018.02.00039>
- Schmetz, J., Pili, P., Tjemkes, S., Just, D., Kerkmann, J., Rota, S., & Ratier, A. (2002). An introduction to Meteosat second generation (MSG). *Bulletin American Meteorology Social*, 83, 977–992. <https://doi.org/10.1175/BAMS-83-7-Schmetz-2>
- Schumann, U., Baumann, R., Baumgardner, D., Bedka, S. T., Duda, D. P., Freudenthaler, V., et al. (2017). Properties of individual contrails: A compilation of observations and some comparisons. *Atmospheric Chemistry and Physics*, 17(1), 403–438. <https://doi.org/10.5194/acp-17-403-2017>
- Schumann, U., & Graf, K. (2013). Aviation-induced cirrus and radiation changes at diurnal timescales. *Journal of Geophysical Research*, 118(5), 2404–2421. <https://doi.org/10.1002/jgrd.50184>
- Schumann, U., Mayer, B., Graf, K., & Mannstein, H. (2012). A parametric radiative forcing model for contrail cirrus. *Journal of Applied Meteorology and Climatology*, 51(6), 1391–1406. <https://doi.org/10.1175/JAMC-D-11-0242.1>
- Schumann, U., Penner, J. E., Chen, Y., Zhou, C., & Graf, K. (2015). Dehydration effects from contrails in a coupled contrail-climate model. *Atmospheric Chemistry and Physics*, 15(19), 11179–11199. <https://doi.org/10.5194/acp-15-11179-2015>
- Shonk, J. K., & Hogan, R. J. (2008). Tripleclouds: An efficient method for representing horizontal cloud inhomogeneity in 1D radiation schemes by using three regions at each height. *Journal of Climate*, 21(11), 2352–2370. <https://doi.org/10.1175/2007jcli1940.1>
- Spezzi, L., Bozzo, A., Jackson, J., Lutz, H. J., do Couto, A. B., Watts, P., et al. (2023). An overview of the enhanced cloud and water vapour products from EUMETSAT new generation imagers. *Remote Sensing of Clouds and the Atmosphere XXVIII*, 12730(2023), 1273002. <https://doi.org/10.1117/12.2679703>
- Stephens, G. L. (1978). Radiation profiles in extended water clouds. II: Parameterization schemes. *Journal of the Atmospheric Sciences*, 35(11), 2123–2132. [https://doi.org/10.1175/1520-0469\(1978\)035<2123:rpiewc>2.0.co;2](https://doi.org/10.1175/1520-0469(1978)035<2123:rpiewc>2.0.co;2)

- Sun, W., & Fu, Q. (2001). Anomalous diffraction theory for randomly oriented nonspherical particles: A comparison between original and simplified solutions. *Journal of Quantitative Spectroscopy & Radiative Transfer*, 70(4–6), 737–747. [https://doi.org/10.1016/s0022-4073\(01\)00042-5](https://doi.org/10.1016/s0022-4073(01)00042-5)
- Teoh, R., Engberg, Z., Shapiro, M., Dray, L., & Stettler, M. E. (2024). The high-resolution Global Aviation emissions Inventory based on ADS-B (GAIA) for 2019–2021. *Atmospheric Chemistry and Physics*, 24(1), 725–744. <https://doi.org/10.5194/acp-24-725-2024>
- Teoh, R., Schumann, U., Majumdar, A., & Stettler, M. E. (2020). Mitigating the climate forcing of aircraft contrails by small-scale diversions and technology adoption. *Environmental Science & Technology*, 54(5), 2941–2950. <https://doi.org/10.1021/acs.est.9b05608>
- Vázquez-Navarro, M., Mannstein, H., & Kox, S. (2015). Contrail life cycle and properties from 1 year of MSG/SEVIRI rapid-scan images. *Atmospheric Chemistry and Physics*, 15, 8739–8749. <https://doi.org/10.5194/acp-15-8739-2015>
- Vázquez-Navarro, M., Mannstein, H., & Mayer, B. (2010). An automatic contrail tracking algorithm. *Atmospheric Measurement Techniques*, 3(4), 1089–1101. <https://doi.org/10.5194/amt-3-1089-2010>
- Voigt, C., Schumann, U., Jessberger, P., Jurkat, T., Petzold, A., Gayet, J. F., et al. (2011). Extinction and optical depth of contrails. *Geophysical Research Letters*, 38(11), L11806. <https://doi.org/10.1029/2011GL047189>
- Wang, Z., Bugliaro, L., Jurkat-Witschas, T., Heller, R., Burkhardt, U., Ziereis, H., et al. (2023). Observations of microphysical properties and radiative effects of a contrail cirrus outbreak over the North Atlantic. *Atmospheric Chemistry and Physics*, 23(3), 1941–1961. <https://doi.org/10.5194/acp-23-1941-2023>
- Wolf, K., Bellouin, N., & Boucher, O. (2023). Sensitivity of cirrus and contrail radiative effect on cloud microphysical and environmental parameters. *Atmospheric Chemistry and Physics*, 23(21), 14003–14037. <https://doi.org/10.5194/acp-23-14003-2023>
- Yi, B., Yang, P., Baum, B. A., L'Ecuyer, T., Oreopoulos, L., Mlawer, E. J., & Liou, K. N. (2013). Influence of ice particle surface roughening on the global cloud radiative effect. *Journal of the Atmospheric Sciences*, 70(9), 2794–2807. <https://doi.org/10.1175/jas-d-13-020.1>